Chapter V

Mechanical property and surface wettability features of IF-type WS_2 nanoparticles dispersed in a polymer

As an important member of the TMDC family, tungsten disulfide (WS_2) has garnered significant research interest recently. To be specific, excellent mechanical, thermal and electronic properties of WS_2 could help extending its usefulness in solid lubricants, lithium batteries, dye-sensitized solar cells (DSSCs), energy storage as well as photocatalysis [1]. Because of the Van der Waals forces along out of plane (*c*-axis) directions, the bonds tend to get sheared when sliding occurs and consequently, coefficient of friction is lowered [2]. This unique capability of sliding one atomic layer over other makes the layered systems (MoS_2 and WS_2) as the most preferred choice in specific applications, such as, solid lubricating agent. Moreover, morphology of these layered systems is likely to influence the quality of lubrication mechanism substantially. Tang *et.al.* have synthesised multi-walled WS_2 nanotubes using fluidized bed method and have investigated their corresponding mechanical properties [3]. The thick WS_2 nanotubes were found to withstand comparatively higher loading amount as compared to the thin WS_2 nanotubes. The layered TMDC compounds, inorganic fullerene (IF) type nanoparticles and inorganic nanotubes (INT) in particular, exhibit excellent mechanical and tribological characteristics owing to their perfect crystalline nature and inclusion of Van der Waals bonding at large [4]. Resembling bucky ball fullerene made of C-atoms, the IF- type WS_2 systems are essentially closed cage nano-dimensional systems with a hollow core within and are usually chemically inert. Earlier it was shown that, adding IF-type WS_2 nanoparticles in a polymer matrix as well as in lubricant oil could enhance the lubricating performance by significant amount [5,6]. Saini *et. al.* have reported the tribological behaviour of electro-deposited Ni-WS_2 composites and showed a remarkable lowering of coefficient of friction from a value of 0.8 to 0.4 at large [5]. On the other hand, Quan *et. al.* have discussed the tribological features of WS_2 solid/liquid systems with trifluorinated-propyl and chlorinated-phenyl with methyl terminated silicone oil (FCPSO) and silahydrocarbons (SiCH) space oils [7]. Their evaluation on WS_2 with SiCH oil exhibited a low and stable coefficient of friction and consequently, durable wear life. Moreover, derived through self-propagating high temperature synthesis (SHS) from using tungsten

and molybdenum powders, nano-lamellar WS_2 and MoS_2 products tend to exhibit much lowered coefficient of friction as compared to their commercially available counterparts [8]. The synthesized product also endorsed better lubricating performance when mixed with oil. Nevertheless, the use of IF- type WS_2 nanoparticles in mechanical and tribological applications is rarely discussed in existing literature.

In this work, we highlight synthesis and characterization of IF-type WS_2 nanoparticles emphasizing structural, thermogravimetric, mechanical and rheological properties at large. A connection between mechanical toughness and coefficient of friction is also sought. Finally, the wettability property of IF-WS_2 nanoparticles dispersed in a low molecular weight polymer has been examined through static and dynamic water contact angle measurements.

5.1 Processing and characterisation of IF-type nano-WS_2/PVA composites

First, 3 g of polyvinyl alcohol (PVA) (low molecular weight, ~11,000 Loba Chemie) is dissolved in 100 mL DI water at a temperature of 80°C, for 4 h. After cooling down to room temperature, as-synthesized WS_2 nano powder is added to the PVA solution under vigorous stirring (~300 rpm), followed by sufficient sonication (frequency~50 kHz) for about 1 h in steps. The blended solution was then spread onto a set of borosilicate glass substrates kept at a temperature of 60°C and in order to help complete evaporation of water, they were left undisturbed for ~12 h. The complete process yielded thick solid films, with homogeneously dispersed IF-type WS_2 nanoparticles. Accordingly, films were casted for three different concentrations of WS_2 nanosystem *viz.* 3%, 6% and 10%. A film without nano-inclusion is also kept ready as reference for comparing mechanical properties with that of loaded ones. It may be noted that, nano-WS_2 dispersed fluids (without film casting) have been employed for evaluating rheological activity and eventually, tribological performance.

As for stress-strain mechanical studies, a universal testing machine (UTM, Zwick, BZ010/TN2S) was employed to examine the tensile strength and toughness of the IF-nano WS_2/PVA films. In contrast, the tribological behavior

was assessed by a Twinedrive™ Rheometer (Anton Paar, MCR 702). The method of study adopted here is the ball on three plate method.

On the other hand, the wettability property of the dispersed systems has beenevaluated with the help of an advanced contact angle meter (Kyowa, DMs-401) set up. The maximum and minimum angles (as regards, advancing and receding angles) have been determined using tilting plate methodology. In this method, the liquid droplet is carefully dropped on the sample, where it is allowed to slide while base tilting was altered between 0° and 90°. For every unit degree of tilting, the contact angles were determined recognizing advancing (θ_{adv}) and receding (θ_{rec}) property. The data acquisition was done with the standard FAMAS software®.

5.2 Structural and morphological analyses

Powder XRD patterns of the pure IF-type WS_2 nanopowder and WS_2 nanoparticle-dispersed PVA films are shown in Fig. 5.1 (A, B). The prominent peak observed at $2\theta \sim 14.45^0$, is attributed to (002) plane of the hexagonal phase of WS_2 (JCPDS File No.08-0237) [9]. Structurally, the crystallites are believed to grow along the *c*-axis, with stacking of numerous (002) planes. Moreover, Bragg's diffraction peaks at 28.34, 32.26, 33.25, 35.20 and 39.33^0 corresponded to the (004), (100), (101), (102) and (103) planes of the hexagonal WS_2; respectively [10]. The average crystallite size (D) of the synthesized nanoparticles has been calculated using the Williamson Hall equation, $\beta cos\theta = 4\epsilon sin\theta + \frac{k\lambda}{D}$, where λ is the wavelength of X-ray radiation, θ is the diffraction angle, β is the line width at half maximum height and ϵ is the mean lattice strain. Plotting a graph between $\beta cos\theta$ vs. $4sin\theta$ and imposing a straight line fit, the mean lattice strain and average crystallite size are calculated from the slope and intercept on the y-axis; respectively (Fig. 5.1 (C)) [11]. The average crystallite size and the lattice

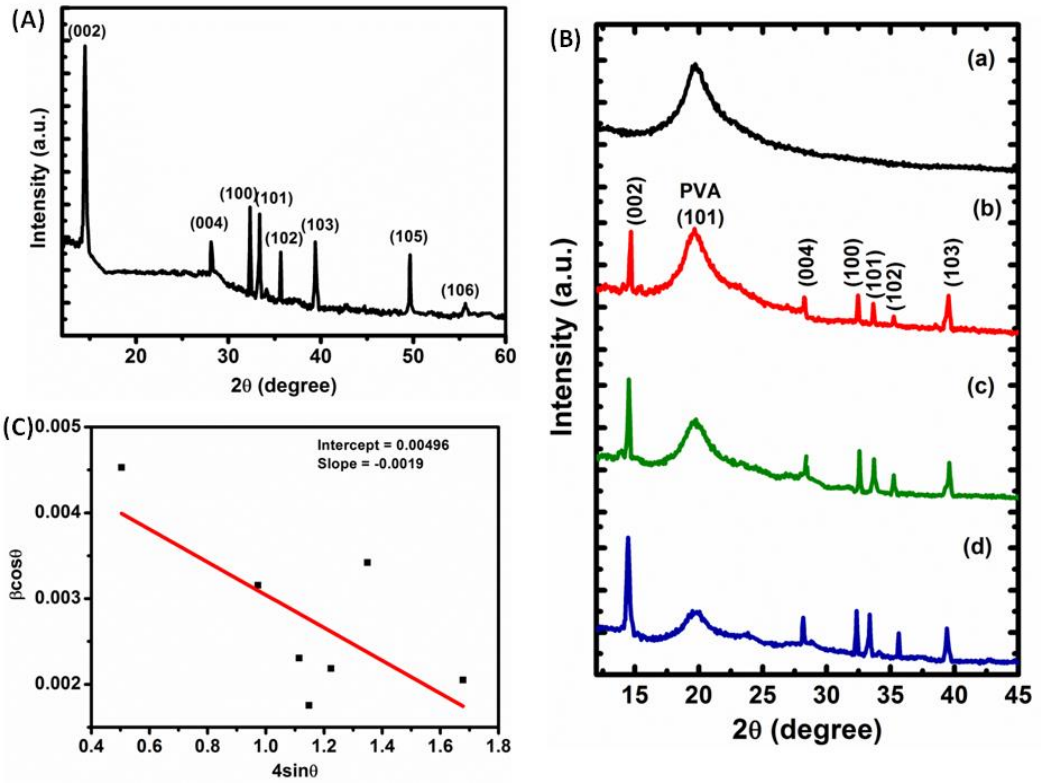

Figure 5.1: XRD plots of (A) IF-type WS_2 nanopowder, (B) IF-WS_2/PVA nanocomposite films with different loading: (a) 0%, (b) 3 %, (c) 6%, (d) 10%. The W-H plot relevant to diffractogram of the IF-WS_2 nanosystem is shown in (C).

strain was found to be 27.4 nm and -1.9×10^{-3}; respectively. Here, the negative value of strain would indicate relaxed nature of the crystallites [12].

With short range ordering, the semi-crystalline nature of PVA is evident from the broad diffraction peak located at ~19.9°, which corresponds the (101) plane of PVA [13]. The IF-WS_2 nanoparticle loaded PVA specimens exhibited suppressed WS_2 peaks due to the presence of polymer environment and lack of compactness. However, with increase in the concentration of the WS_2 nanoparticles, the peak intensity tends to improve significantly (Fig. 5.1 B (c)), thereby indicating an increase in the crystallinity content [14]. Consequently, a decrease in the peak intensity of PVA was noticeable due to a lowered degree of crystallinity of PVA. The loading of IF-WS_2 nanoparticles causes a lowering in the intermolecular interaction between the PVA chains contributing to more amorphous nature at large [15].

To ensure a uniform dispersion of the nanoparticles in PVA, imaging through SEM was performed on different specimens, which can be found in Fig. 5.2 A (a-f). The upper and lower panel of sub-figures essentially indicate views at different magnifications. From the micrographs, it can be witnessed that, the interparticle separation is comparatively large when nanoparticle concentration is kept low. Moreover, with increase in IF-type WS_2 content, the agglomeration of nanoparticles increases and attains its maximum for 10wt% nano-WS_2 loading. The clustering through assimilation of the nanoparticles occurred in order to minimize the overall surface energy in the confined environment [15]. Apparently, 6 wt% loading of IF-type WS_2 gave a fairly good dispersity owing to homogenous distribution and minimal clustering. Low and high resolution TEM images of the IF-WS_2 nanosystems are shown in Fig. 5.2 B (a-c). The balloon shaped structures are essentially particles that possess polyhedral entities with a hollow core at the centre, representing the most-suited IF- type nanostructure [16]. One can notice a shadowed impression of a few particles through the WS_2 nanoparticle due to their presence in successive imaging planes (Fig. 5.2 B (a,b)). The average size of the IF-WS_2 nano particles is quite large, and in the range of 80 - 160 nm with a non-spherical core dimension in the range of 55-75 nm. Apart from a hollow core within, note the typical bending of lattices at the IF-WS_2 nanoparticle surfaces, which is generally found to be obtuse (Fig. 5.2 B (c)). Resembling carbon- based bucky ball fullerene structure, it is the regular polyhedral structure with a central core inside and adjoining edges that would create facets outside gives the terminology, IF-type system. Moreover, the SAED pattern is shown as inset of Fig. 5.2 B (a). With diffused ring patterns, the SAED pattern depicts the polycrystalline nature of the synthesized nanosystem. The interplanar spacing is calculated using the *ImageJ*® software and found to be ~0.62 nm.

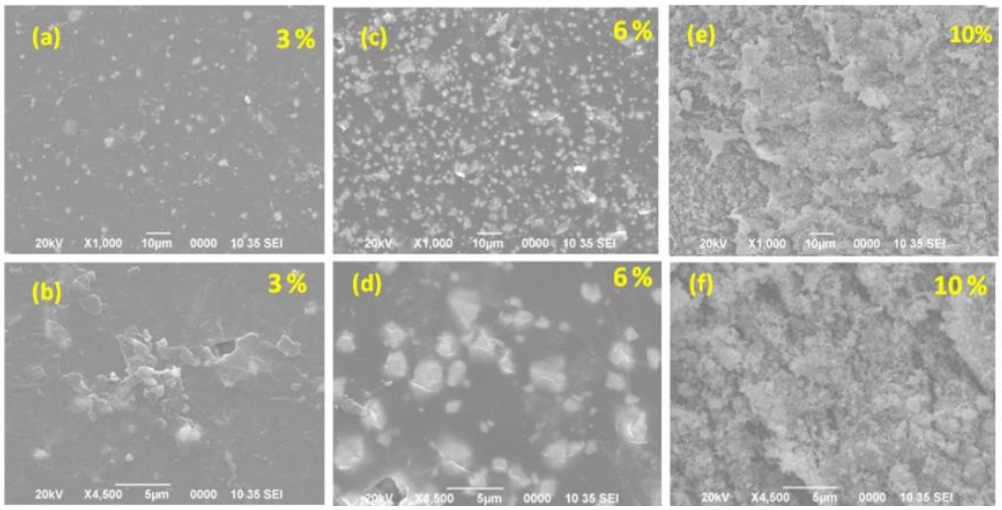

Figure 5.2 (A)**:** SEM images of IF-WS_2/PVA solid films with different nanoparticle loading: (a) 3%, (b) 6% and (c) 10%. The magnified images are shown in (d), (e) and (f); respectively.

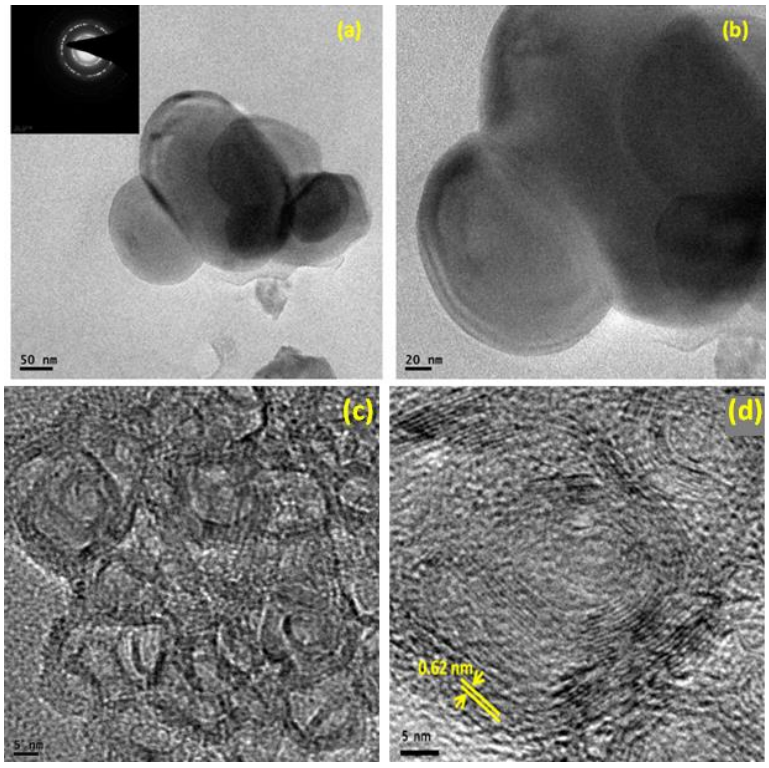

Figure 5.2 (B): TEM micrographs of the IF-WS_2 nanoparticles at (a) lower magnification, (b,c) higher magnification, and (d) enlarged IF-type WS_2 highlighting interplanar spacing and bending at the surface. SAED pattern is shown as inset of (a).

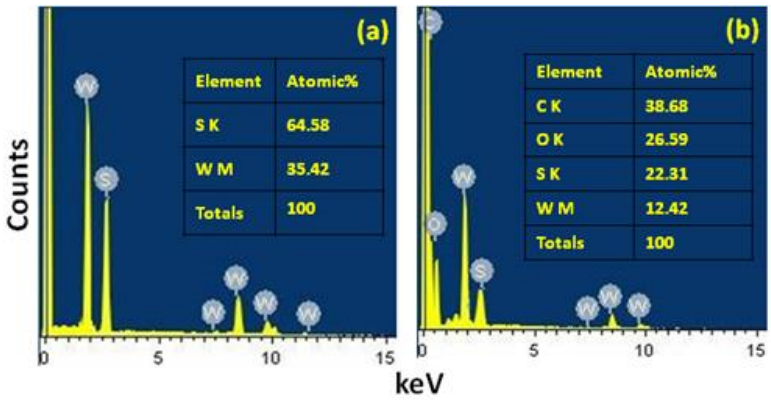

Figure 5.2 (C): EDX spectra of (a) IF-WS_2 only and (b) IF-WS_2/PVA composite film (6 wt% loading).

The EDX spectra of the pure WS_2 nanopowder and WS_2-PVA nanocomposite films are shown in Fig. 5.2 C. The presence of elements W and S can be clearly witnessed in the spectra. As regards quantitative information, the ratio of S- to-W stands at 1.85:1 in pure WS_2 powder and 1.79:1 in WS_2/PVA nanocomposite system, at 6 wt% loading. Availability of a slightly less content of sulphur could be due to the loss of unsaturated S atoms from the nanoparticle surfaces. Thus sulphur vacancies are largely expected in the system. In IF-type WS_2 nanoparticle dispersed PVA specimen, apart from the peaks that arise due to W and S elements, a characteristic O-peak has been witnessed. The elements H and C are not identifiable in the EDX spectra, though the latter's contribution near zero-line could emerge from conducting carbon-tape used to fix the working specimen.

5.3 FT-IR spectroscopy and thermo-gravimetric studies

Different vibrational modes present in the nano-WS_2/PVA specimens under study have been revealed through the Fourier transform infrared spectroscopy (FTIR), the results of which are shown in Fig. 5.3.

In the FTIR spectrum of the pure WS_2, the band located at 460 cm^{-1} is attributed to the S-S bond [1]. Whereas, the bands at 680 cm^{-1} and 857 cm^{-1} are due to the W-S stretching and bending vibrations; respectively [17, 18]. Moreover, the peaks at 1453 and 1640 cm^{-1} can be ascribed to the stretching

deformation of the hydroxyl group and also witnessed for PVA without nano inclusion [17]. A prominent band at 1097 cm^{-1} corresponds to C-O stretching vibration of acetyl group present in the PVA network [19]. The peaks at ~2853 cm^{-1} and 2925 cm^{-1} are believed to have originated from asymmetric and symmetric C-H stretching vibrations; respectively [20]. On the other hand, in the FTIR spectrum of the IF-type WS_2/PVA nanocomposite film, the peak at ~ 460 cm^{-1} is assigned to the S-S bond [1], whereas the respective bands at ~697 cm^{-1} and 857 cm^{-1} are attributed to the W-S stretching and bending vibrations [17, 18]. The bands found at ~1463 and 1640 cm^{-1} are due to the stretching vibrations of the hydroxyl group present in PVA in consistency with an earlier report [17]. The peaks at ~2851 and 2914 cm^{-1} are due to manifested asymmetric and symmetric C-H vibrations; respectively [20]. Since all the peaks present in the FTIR spectra of pure WS_2 and pure PVA are present in IF-type/PVA nanocomposites with slight variation in wavenumber positions, it can be concluded that the WS_2 is homogeneously dispersed in the PVA network.

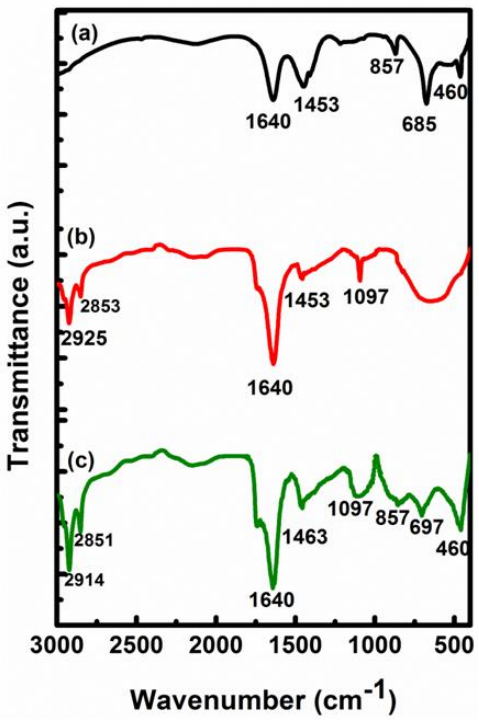

Figure 5.3: FT-IR spectra of (a) pure PVA, (b) pure IF-WS_2 and (c) IF-WS_2/PVA nanocomposites.

The thermal stability of pure nano-WS_2, pure PVA and WS_2/PVA nano-composites has been evaluated by using TGA equipment under nitrogen atmosphere, the results being shown in Fig. 5.4. As can be found, the weight loss of pure IF- type WS_2 starts at ~350^oC, beyond which the loss is rapid upto a temperature of 480 °C (Fig. 5.4 (a)). The total weight loss of WS_2 is about 6.45 % when it is heated to a temperature of 650^oC. This weight loss is attributed to the substantial removal of sulphur and subsequent oxidation of IF-type WS_2 to yield stable WO_3 [20]. Between the temperature range 480-650^oC, no further loss of weight of nano-WS_2 has been observed which suggests complete conversion of WS_2 to WO_3 [20]. The thermal decomposition of the PVA and nano-WS_2/PVA nanocomposites are plotted in Fig. 5.4 (b). The decomposition of PVA was observed along three steps over different temperature ranges [21]. In the first step, before reaching a temperature of 160^oC PVA loses its mass (about 9wt%) essentially through primary decomposition and the release of absorbed water owing to hydrophilic nature of the PVA polymer. The sharp decrease in the TGA curve observed between 260^oC and 420^oC characterizes ~68% weight loss and was attributed to the degradation of –OH groups attached to the side chains of the PVA molecules. In the third step, between 430–520^oC, the weight loss is ascribed to the complete carbonization of PVA structure. Above 520^oC, PVA was converted to carbon and carbonaceous product, which is stable over a range of 520–600^oC [21]. The inclusion of nanoscale IF-WS_2 into PVA was seen to improve thermal stability, especially at higher temperature. The temperature range at which 5%, 10%, 50% and 70% degradation of the nanocomposite films occur are highlighted in Table 5.1. Our results indicate that, incorporation of nano-WS_2 into PVA is capable of restricting thermal degradation/disruption of molecular chains. This can be attributed to the strong surface interactions between the nanoscale WS_2 and PVA, such as hydrogen bonding and the physical barrier effect of the IF- type WS_2 and also observed for a similar system earlier [22].

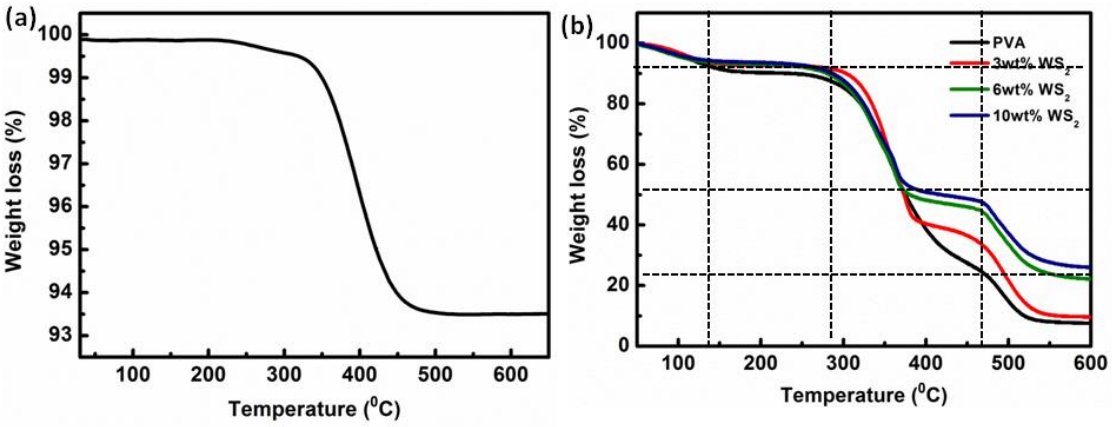

Figure 5.4: TGA plots of (a) pure IF-type WS_2 and (b) pure PVA and specimens with nano-WS_2 loading at different wt%.

Table 5.1: Physical parameters related to theromogravimetric weight loss for nanocomposite systems

Specimen	$T_{(5\%)}$	$T_{(10\%)}$	$T_{(50\%)}$	$T_{(70\%)}$
PVA	112 ^{o}C	245 ^{o}C	375 ^{o}C	430 ^{o}C
(3wt%) IF-WS_2/PVA	121 ^{o}C	304 ^{o}C	373 ^{o}C	480 ^{o}C
(6wt%) IF-WS_2/PVA	108 ^{o}C	280 ^{o}C	381 ^{o}C	510 ^{o}C
(10 wt%) IF-WS_2/PVA	115 ^{o}C	288 ^{o}C	408 ^{o}C	528 ^{o}C

5.4 Mechanical and tribological features

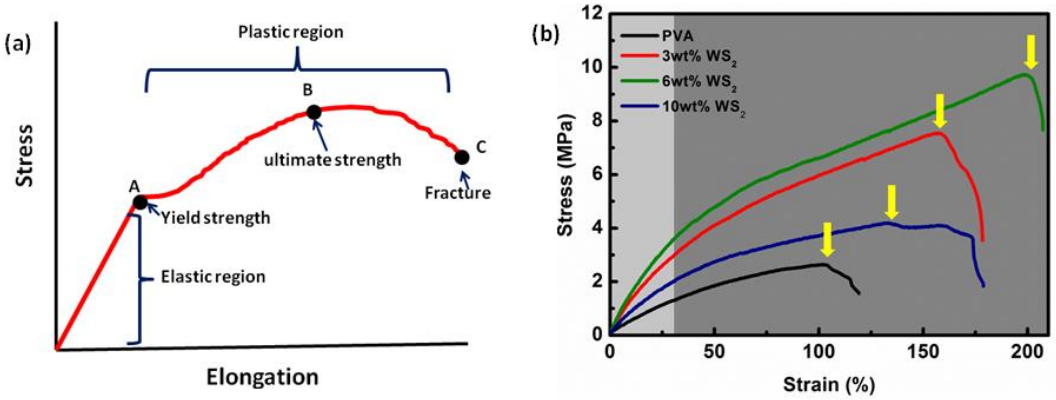

Figure 5.5: (a) Schematic curve of stress strain relationship (b) actual stress-strain plots measured for pure PVA and IF-WS_2 nanocomposites at different wt% of WS_2 loading.

The mechanical properties of the IF-type WS_2-PVA nanocomposite films were investigated using a universal testing machine (UTM) (Zwick, BZ010/TN2S). The stress-strain responses of the samples are shown in Fig. 5.5 (a,b). As can be found, the plots essentially characterize elastic and pseudo-plastic segments before reaching the breaking point. The mechanical properties, such as, tensile strength, Young's modulus and ductility of the nanocomposite films tend to increase noticeably as compared to the pure PVA film.

The enhancement of mechanical properties, however, is prominent up to 6wt% inclusion of nanoscale IF-WS_2. The toughness also follows the similar trend as other mechanical properties. Surprisingly, mechanical feature is hindered for excessive loading (10 wt%) of WS_2 nanoparticles, which can be explained by the phenomenon of agglomeration [23]. With higher amounts of nanoparticles, the dispersion of IF-type WS_2 becomes inadequate with less free volume available for the dispersed nanoparticles. As a result, the agglomeration might impede deformation and result in local stress concentration [23] and this eventually, leads to the reduction in elongation and toughness. The mechanical properties of the composite films are enlisted in Table 5.2.

Table 5.2: Physical parameters of nanocomposite films determined through UTM

Specimen	Breaking stress, σ_{max} (MPa)	Elongation, ϵ (%)	Young's modulus, Y (kPa)	Toughness (MPa)	Thickness (mm)
PVA	2.62	102.22	0.0419	212.5	0.17 ± 0.01
(3 wt%) IF-WS_2/PVA	7.51	158	0.0962	900	0.15 ± 0.01
(6wt%) IF-WS_2/PVA	9.77	199	0.1121	1315	0.13 ± 0.01
(10 wt%) IF-WS_2/PVA	4.18	133	0.06125	551.9	0.14 ± 0.01

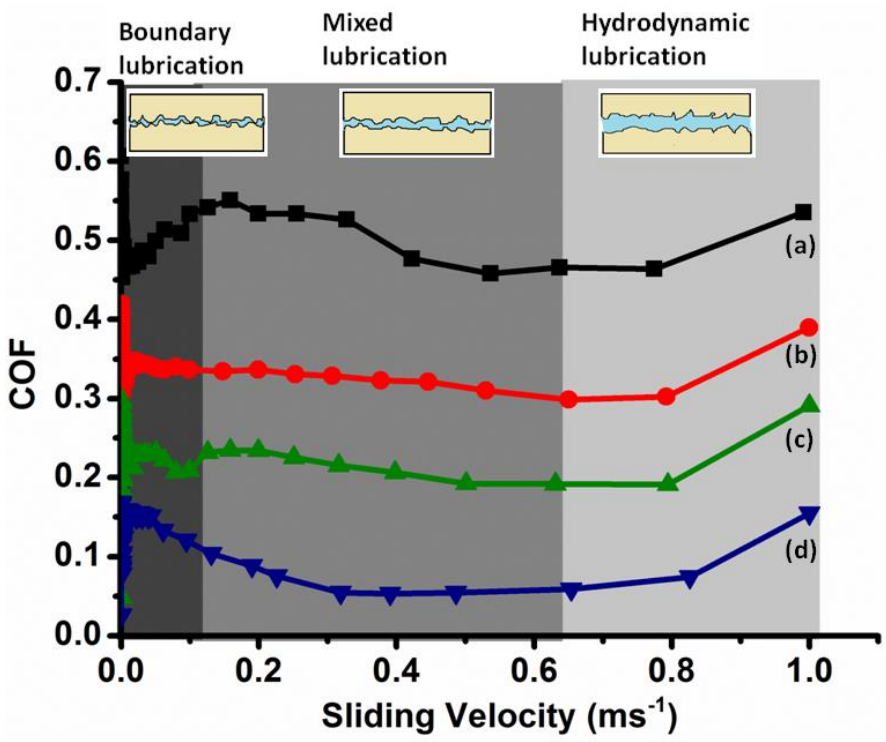

Figure 5.6: Stribeck curves for pure PVA and IF-WS_2/PVA nanocomposites for (a) pure PVA, and PVA with nano IF-WS_2 at (b) 3wt%, (c) 6wt% and (d) 10wt% loading.

On the other hand, the ball on three plate method was performed to evaluate the tribological behaviour of pure PVA and IF-type WS_2/PVA nanocomposites, for which solution was used instead of solid films. Fig 5.6 represents a series of Stribeck curves for the pure PVA and the nano-WS_2/PVA composites. The Stribeck curve essentially gives the relationship between Hersey number and the coefficient of friction of a given fluid. The Hersey number is the dimensionless number obtained from the velocity (v) times the dynamic viscosity (η) divided by the load per unit length of bearing (P) i.e., $\frac{v.\,\eta}{P}$. For a given viscosity and load, the Stribeck curve shows how the coefficient of friction (COF) responds to an increasing velocity [24]. As shown in Fig. 5.6, the whole region along the X-axis can be divided into three distinct parts. For instance, first one is the region of low velocity and high loading. It is called as the boundary lubricating region, where the sliding speed is very low and the contact between the friction partners is solid contact, the wear could be high in this particular region. The second region is the mixed lubricating region, in which the sliding speed is not that high. Here

the approach is partial solid contact and consequently, wear is substantially moderate. The final region starts from the point of lowest COF value. It is the high velocity low loading region, called as the hydrodynamic lubricating region. In this region, owing to very high sliding velocity a lubrication film is developed between the contact points, and thus offers least wear. It was observed that incorporation of IF-type WS_2 nanoparticles is capable of lowering the COF significantly. Moreover, this decrement becomes more prominent with the increasing IF-type WS_2 loading. The nano-IF-WS_2 can provide an effective rolling friction mechanism and serve as spacers, preventing asperity contact between the mating surfaces [25]. The low friction of WS_2 arises from the van der Waal's bonding present between different WS_2 planes, which help one plane to slide over the other. Both rolling and sliding friction contribute largely to suppress the overall friction after inclusion of nanosystems of IF-type [25, 26]. The rolling, sliding and exfoliation friction mechanisms are described schematically in Fig. 5.7.

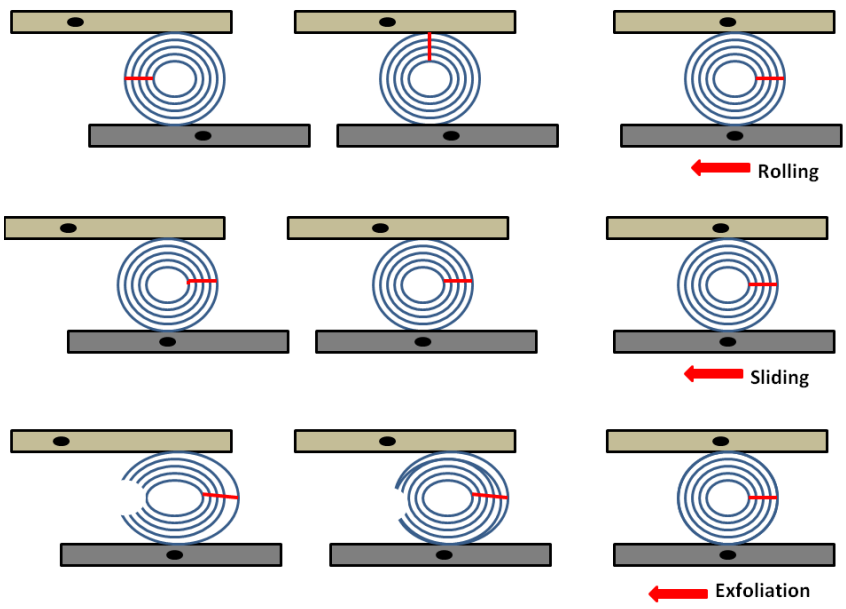

Figure 5.7: Schematic representation of the three friction mechanisms of IF- particles rolling, sliding and exfoliation (source: [26]).

5.5 Surface wettability features of nano-WS_2-dispersed PVA films

The water contact angles (CA) of PVA, and nanoscale IF- type WS_2 loaded PVA (3-10 wt%) are shown in Fig. 5.8 (a-d). To be specific, exhibiting a hydrophilic response the PVA film gives a stable CA value of 68.1°, whereas, nanoscale IF-type WS_2 loaded films predicted CA values of ~85.2°, 92° and 113.9°. It is quite apparent that, with an increasing content of nano-WS_2, the CAs tend to rise owing to an increased surface roughness [27]. As a result, a hydrophilic to hydrophobic surface characteristics can be ensured with the inclusion of WS_2 nanoparticles. It was believed that the hydrophobic behaviour is a consequence of increased surface roughness of the films, as predicted in an earlier work [28]. The loading of nano-IF type WS_2 systems in polymeric host is likely to induce local deformation around the particles and consequently, may influence the surface structure drastically (lower panel, Fig. 5.8). The presence of localized organic-inorganic matter interface is believed to be the origin of surface roughness which could enhance the CA values by appreciable amounts (Table 5.3A).

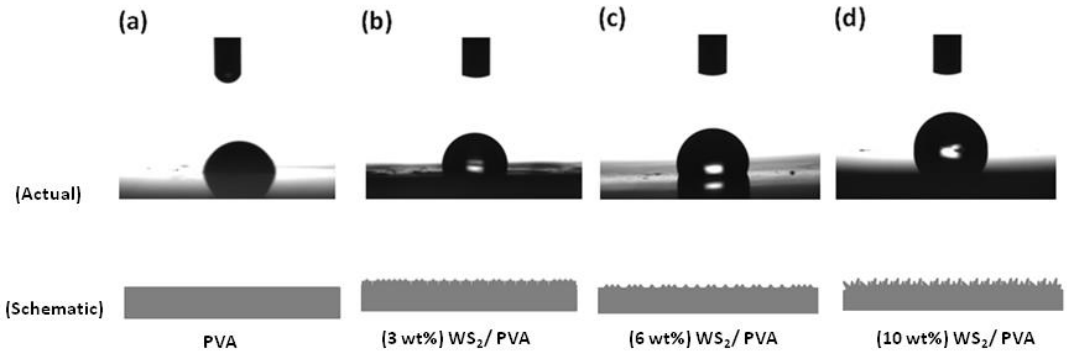

Figure 5.8: Static water contact angle snap-shots for (a) pure PVA, and PVA with nano IF-WS_2 at (b) 3wt%, (c) 6wt% and (d) 10wt% loading.

Table 5.3 A: Wetting-dewetting phenomena: Contact angle (CA) parameter and CA hysteresis measured at the nanocomposite film surfaces

Specimen	Contact angle (°)		CAH (°)	Critical angles, α_1 (°), α_2 (°)
	Advancing	Receding		
PVA	74 ± 0.39	38 ± 0.54	36	--
(3 wt%) IF-WS_2/PVA	90 ± 0.35	56 ± 0.41	34	--
(6wt%) IF-WS_2/PVA	95 ± 0.42	66 ± 0.44	29	24, 45
(10 wt%) IF-WS_2/PVA	122 ± 0.28	102 ± 0.31	20	43, 61

Contact angle hysteresis (CAH) is an important parameter for understanding surface wettability features of a given specimen under study. For measuring CAH value, the droplet is allowed to slide over the surface of the specimen while employing tilting plate methodology. As a result of sliding, the droplet undergoes numerous changes in the contact line, which leads to several CA values (Fig. 5.9). Theoretically, it was explained by assuming that the Gibbs energy of a system has multiple minima and a single global minimum, considering the fact that each value of the allowed CA indicates the metastable state of the system [29]. The maximum and minimum CAs are invariably recognized as, advancing (θ_{adv}) and receding (θ_{rec}) angles and subsequently, the difference between these values give the exact CAH value. At certain degree of tilting, some critical angles are defined which give an idea regarding change of contact line [30]. On the surface, the angles at which the first displacement of the contact line of the water droplet occurs and the angle for which both the uphill and downhill contact line of the water droplet changes are known as critical angles, α_1 and α_2, respectively [29]. Whereas black and red curves refer to respective variations in θ_{adv} and θ_{rec}, the blue-curve depicts a change of the CAH. Dictated by surface roughness feature herein, here, we noticed an enhanced static CA with an increased dispersion of nano-WS_2 content (Fig. 5.9, Table 5.3A),

but with undulated θ_{adv} and θ_{rec} values when subjected to tilting of the base (Fig. 5.9 lower panel). Furthermore, even though the CAH value offers a steady growing trend with tilting angle, the overall CAH is lowered with nano-WS_2 dispersion (Fig. 5.9, Table 5.3B). Opposite to the "*Petal effect*" where a high CA and high CAH can be noticed, a higher CA and lower CAH is essentially associated with the phenomenon called "*Lotus effect*" where solid-liquid surface adhesion property is suppressed drastically [30-32]. Thus, we can say that, while assuming latter type effect the hydrophobic response is effectively improved upon addition of nano-WS_2 into PVA. The schematic view of the droplet shape imposed by surface wettability and as a consequence of base tilting is presented in the lower panel of Fig. 5.9. Note the shape-deformation at both the extremes with and without base-tilting.

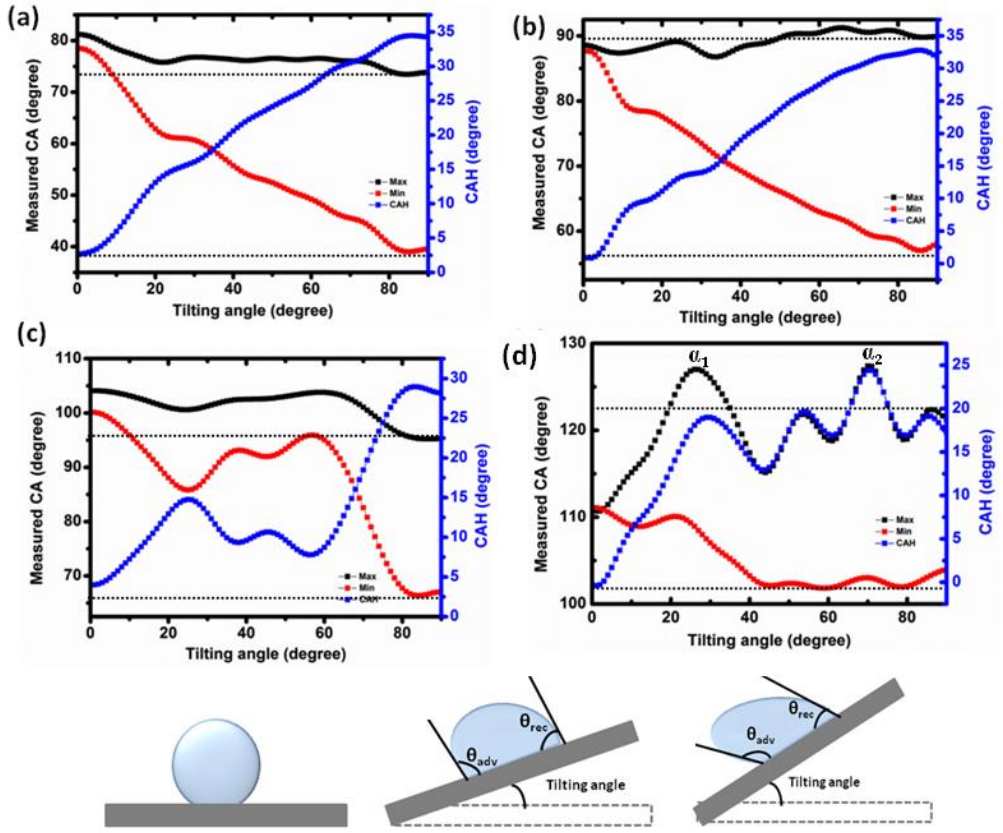

Figure 5.9: Dynamic CA hysteresis obtained for different films: (a) PVA only, and PVA with nano IF-WS_2 inclusions at (b) 3% wt%, (c) 6 wt% and (d) 10 wt% loading.

We have also estimated surface energy of the nanoscale IF-type WS_2/PVA films considering water (L_1) and ethylene glycol (L_2) as the reference liquids. According to Kaelble Uy model [33], one can split the surface tension into two components: polar and dispersive, because of the independent interactions of the solid and solvent [34]. The total surface energy of the nanocomposite film is given by,

$$\gamma_s^{tot} = \gamma_s^d + \gamma_s^p \quad , \qquad (5.1)$$

where, γ_s^d and γ_s^p are the dispersive and polar components of the solid.

The dispersive component arises due to the interaction of the temporary fluctuations of the charge distribution in the atoms or molecules, whereas, the polar component arises as a result of the coloumb interaction between the permanent dipoles and between permanent and induced dipoles.

The equations which govern the aforementioned theory are given by:

$$a_1 x + b_1 y = d_1 \qquad (5.2)$$

$$a_2 x + b_2 y = d_2, \quad x \geq 0, y \geq 0 \qquad (5.3)$$

with symbolic representations, $x \equiv \sqrt{\gamma_s^d}$ and $y \equiv \sqrt{\gamma_s^p}$,

and $a_1 = \sqrt{\gamma_{L_1}^d}$ and $b_1 = \sqrt{\gamma_{L_1}^p}$, $d_1 = \frac{\gamma_{L_1}^{tot}(1+Cos\theta_{L_1})}{2}$

$a_2 = \sqrt{\gamma_{L_2}^d}$ and $b_2 = \sqrt{\gamma_{L_2}^p}$, $d_1 = \frac{\gamma_{L_2}^{tot}(1+Cos\theta_{L_2})}{2}$.

For water, $\gamma_{L_1}^d = 22.1$, $\gamma_{L_1}^p = 50.7$ (SFE database, Kyowa Interface Science Co. Ltd.)

and therefore, $\gamma_{L_1}^{tot} = 72.8$. For ethylene glycol, $\gamma_{L_2}^d = 29.4$, $\gamma_{L_2}^p = 18.3$ [35] and $\gamma_{L_2}^{tot} = 47.7$.

Putting the required values for each of the specimens under study in equations 5.2 and 5.3, the surface energy of the nano-WS_2 dispersed systems have been calculated. The values of $\theta_{L_1}, \theta_{L_2}$ as well as calculated surface energy values are shown in Table 5.3 B. It is worth mentioning here that, while polar component falls, dispersive component improves with nanoparticle inclusion but eventually, total surface energy gets lowered substantially. To be specific, for a

pure PVA and 10% IF-type WS_2/PVA film, the surface energies are computed as, 37.4 and 24.7 mJ/m^2. The variation of total surface energy, polar component of surface energy and dispersive component of surface energy for different wt% loading of IF-WS_2 in PVA is plotted in Fig.5.10. A marginal drop in total surface energy, an improved hydrophobic (dewetting) feature and lowered adhesion are believed to have originated from microscopic manifestation in surface structure locally after inclusion of nanoparticles in the PVA host.

Table 5.3 B: Wetting-dewetting phenomena: Surface energy measured at the nanocomposite film surfaces

Sample	Water CA (°)	Ethylene glycol CA (°)	Surface energy (polar) (mJ/m^2)	Surface energy (dispersive) (mJ/m^2)	Total surface energy (mJ/m^2)
PVA	64.3	49.1	9.79	27.67	37.46
(3 wt%) IF-WS_2/PVA	85.2	52.1	3.06	32.94	36
(6wt%) IF-WS_2/PVA	92	61.2	1.66	30.47	32.13
(10 wt%) IF-WS_2/PVA	107	78	0.442	24.30	24.74

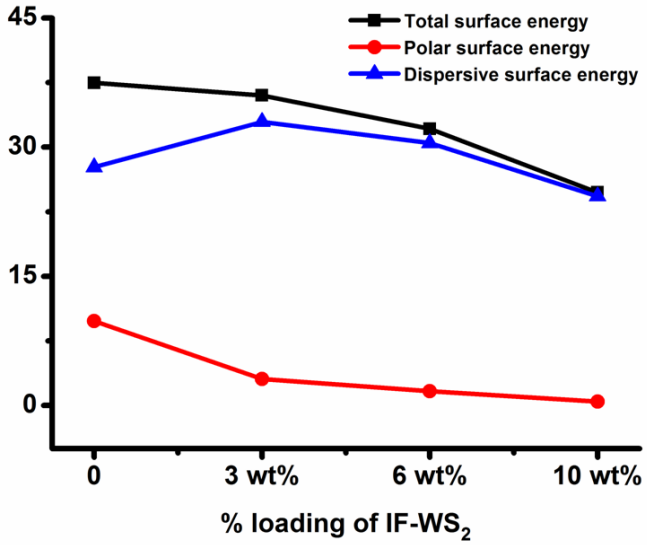

Figure 5.10: Curve showing the variation of total surface energy, polar component of surface energy and dispersive component of surface energy for different wt% loading of IF-WS_2 in PVA.

5.6 Conclusion

In this work, we have demonstrated structural, mechanical and wettability characteristics of hydrothermally processed IF-type WS_2 nanoparticles, homogeneously dispersed in a polymer host. The polyhedral, fullerene like nanostructures of WS_2 with a hollow core inside are quite evident from TEM imaging. The range of elastic and plastic regions was observed to be dependent on the amount of nanoparticle loading. For nanocomposite films, elongation and consequently, Young's modulus of elasticity generally offers an increasing trend but maximal value was seen for 6 wt% nano-WS_2 loading. Breaking stress also gives an enhanced value, from 2.7 to 9.7 MPa, without and with 6wt% loading of nano-WS_2. Moreover, tribological studies have revealed a significantly lowered COF with inclusion of nano-WS_2. Thermally and mechanically stable nanocomposite films also presented excellent hydrophobic response by displaying high CA but reduced CAH. Surface energies of the composite films have been calculated by considering contributions from the polar and dispersive parts separately for two reference liquids. The net surface energy was found to vary in the range of 24.7 to 37.5 mJ/m^2.. Bifunctional mechanical and hydrophobic features have immense scope in coating, sealing and textile industries apart from nano-mechanical components.

References

[1] Panigrahi, P. K., Pathak A. Microwave-assisted synthesis of WS_2 nanowires through tetrathiotungstate precursors. *Science and Technology of Advanced Materials*, 9:045008 (6pp), (2008).

[1] Wang, H., Xu, B., Liu, J. Micro and nano sulfide solid lubrication, 1st edition, Science Press Beijing and Springer-Verlag Berlin Heidelberg, 2012.

[2] Tang, D-M., Wei, X., Wang, M-S., Kawamoto, N., Bando, Y., Zhi, C., Mitome, M., Zak, A., Tenne, R., Golberg, D. Revealing the anomalous tensile properties of WS_2 nanotubes by in situ transmission electron microscopy. *Nano Letters*, 13:1034-40, 2013.

[3] Ashiri I. K-., Tenne, R. On the mechanical properties of WS_2 and MoS_2 nanotubes and fullerene-like nanoparticles: in situ electron microscopy measurements. *The Journal of the Minerals, Metals and Materials Society*, 68:151-167, 2016.

[4] Yang, H., Liu, S., Li, J., Li, M., Peng, G., Zou, G. Synthesis of inorganic fullerene-like WS_2 nanoparticles and their lubricating performance. *Nanotechnology*, 17:1512, 2006.

[5] Saini, R., Roy, D., Das, A. K., Dixit, A. R, Nayak, G. C. Tribological behaviour and characterisation of Ni-WS_2 composite coating. *International Journal of Surface Science and Engineering*, 10:240-252, 2016.

[6] Quan, X., Gao, X., Weng, L., Hu, M., Jiang, D., Wang, D., Sun, J., Liu, W. Tribological behavior of WS_2-based solid/liquid lubricating systems dominated by surface property of WS_2 crystallographic planes. *RSC Advances*, 5:64892-64901, 2015.

[7] An, V., Irtegov, Y., Izarra, C. de. Study of tribological properties of nanolamellar WS_2 and MoS_2 as additives to lubricants. *Journal of Nanomaterials*, Article ID 865839, 8 pages, 2014.

[8] Hazarika, S. J., Mohanta, D. Inorganic fullerene-type WS_2 nanoparticles: processing, characterization and its photocatalytic performance on malachite green. *Applied Physics A*, 123:381-391, 2017.

[9] Joly-Pottuz, L., Dassenoy, F., Belin, M., Vacher, B., Martin, J.M., Fleischer, N. Ultralow-friction and wear properties of IF-WS_2 under boundary lubrication. *Tribology Letters*, 18:477-485, 2005.

[10] Park, S. W., Jang, J. T., Cheon, J., Lee, H. H., Lee, D. R., Lee, Y. Shape-dependent compressibility of TiO_2 anatase nanoparticles. *Journal of Physical Chemistry C*,112(26): 9627-9631, 2008.

[11] Hazarika, S., Mohanta, D. Extraction and characterization of mixed phase KNO_2–KNO_3 nanocrystals derived from flat-leaf green spinach. *Physica Scripta*, 87:015603-1–5, 2013.

[12] Rao, J. K., Raizada, A., Ganguly, D., Mankad, M. M., Satyanarayana, S. V., Madhu, G. M. Enhanced mechanical properties of polyvinyl alcohol

composite films containing copper oxide nanoparticles as filler. *Polymer Bulletin*, 72:2033-2047, 2015.

[13] Xiao-Dong, M., Xue-Feng, Q., Jie, Y., Kang, Z.-, Zhu, F. Preparation and characterization of polyvinyl alcohol–selenide nanocomposites at room temperature. *Journal of Material Chemistry*, 12:663-666, 2002.

[14] Hemalatha, K. S., Rukmani, K., Suriyamurthy, N., Nagabhushana, B. M. Synthesis, characterization and optical properties of hybrid PVA–ZnO nanocomposite: A composition dependent study. *Materials Reserach Bulletin*, 51:438-446, 2014.

[15] Díez-Pascual, A. M., Naffakh, M., Marco, C., Ellis, G. Rheological and tribological properties of carbon nanotube/thermoplastic nanocomposites incorporating inorganic fullerene-Like WS_2 nanoparticles. *Journal of Physical Chemistry B*, 116:7959-7969, 2012.

[16] Vattikuti, S. V. P., Byon, C., Chitturi, V. Selective hydrothermally synthesis of hexagonal WS_2 platelets and their photocatalytic performance under visible light irradiation. *Superlattices and Microstructures*, 94:39-50, 2016.

[17] Wu, J., Yue, G., Xiao, Y., Huang, M., Lin, J., Fan, L., Lan, Z., Lin, J-Y. Glucose aided preparation of tungsten sulfide/multi-wall carbon nanotube hybrid and use as counter electrode in dye-sensitized solar cells. *ACS Applied Materials & Interfaces*, 4:6530-6536, 2012.

[18] Kim, S-K., Wie, J. J., Mahmood, Q., Park, H. S. Anomalous nanoinclusion effects of 2D MoS_2 and WS_2 nanosheets on the mechanical stiffness of polymer nanocomposites. *Nanoscale*, 6:7430-5, 2014.

[19] Xu, F., Almeida, T. P., Chang, H., Xia, Y., Wears, M. L., Zhu, Y. Multi-walled carbon/IF-WS_2 nanoparticles with improved thermal properties. *Nanoscale*, 5:10504-10, 2013.

[20] Khare, P., Ramkumar, J., Verma, N. Control of bacterial growth in water using novel laser-ablated metal–carbon–polymer nanocomposite-based microchannels. *Chemical Engineering Journal* , 276:65-74, 2015.

[21] Zhou, K., Jiang, S., Bao, C., Song, L., Wang, B., Tang, G., Hu, Y., Gui, Z. Preparation of poly(vinyl alcohol) nanocomposites with molybdenum

disulfide (MoS_2): structural characteristics and markedly enhanced properties. *RSC Advances*, 2:11695-11703, 2012.

[22] Xu, F., Yan, C., Shyng, Y-T., Chang, H., Xia, Y., Zhu, Y. Ultra-toughened nylon 12 nanocomposites reinforced with IF-WS_2. *Nanotechnology*, 25:325701-1-10, 2014.

[23] Zhu, D., Wang, J., Wang, Q. J. On the Stribeck Curves for Lubricated Counterformal Contacts of Rough Surfaces, *Journal of Tribology*, 137:021501-1-10, 2015.

[24] Lecina, E. G-., García-Urrutia, I., Díez, J. A., Fornell, J., Pellicer, E., Sort, J. Codeposition of inorganic fullerene-like WS_2 nanoparticles in an electrodeposited nickel matrix under the influence of ultrasonic agitation. *Electrochimica Acta*, 114:859-867, 2013.

[25] Tevet, O., Von-Huth, P., Popovitz-Biro, R., Rosentsveig, R., Wagner, H. D., Tenne, R. Friction mechanism of individual multilayered nanoparticles. *Proceedings of National Academy of Sciences*, 108:19901-19906, 2011.

[26] Hou, X., Deem, P. T., Choy, K-L. Hydrophobicity study of polytetrafluoroethylene nanocomposite films. *Thin Solid Films*, 520:4916-4920, 2012.

[27] Yang, C., Tartaglino, U., Persson, B. N. J. Influence of Surface Roughness on Superhydrophobicity. *Physical Review Letters*, 97:116103, 2006.

[28] White, J. A., Santos, M. J., Rodríguez-Valverde, M. A., Velasco, S. Numerical study of the most stable contact angle of drops on tilted surfaces. *Langmuir*, 31:5326-5332, 2015.

[29] Aideo, S. N., Mohanta, D. Surface-wettability and Structural Colouration Property of Certain *Rosaceae* Cultivars With Off-to-dark Pink Appearances. *Journal of Bionic Engineering*, 15:1012, 2018.

[30] Nosonovsky, M. Model for solid-liquid and solid-solid friction of rough surfaces with adhesion hysteresis. *Journal of Chemical Physics*, 126:224701, 2007.

[31] Nosonovsky, M., Bhushan, B.. *Green Tribology: Green Energy and Technology*, Springer-Verlag, Berlin, Heidelberg, 2012.

[32] Kaelble, D.H., Uy, K.C. A reinterpretation of organic liquid polytetrafluoroethylene surface interactions. *Journal of Adhesion*, 2:50-60, 1970.

[33] Shen, J., He, Y., Wu, J., Gao, C., Keyshar, K., Zhang, X., Yang, Y., Ye, M., Vajtai, R., Lou, J., Ajayan, P. M. Liquid phase exfoliation of two-dimensional materials by directly probing and matching surface tension components. *Nano Letters*, 15:5449-5454, 2015.

[34] Kawai, A. *Journal of the Physical Society of Japan*, 34:191, 1998.